nature materials

ARTICLES

https://doi.org/10.1038/s41563-020-0789-2

Check for updates

A bioinspired and hierarchically structured shape-memory material

Luca Cera[1], Grant M. Gonzalez[1], Qihan Liu[1], Suji Choi[1], Christophe O. Chantre[1], Juncheol Lee[2], Rudy Gabardi[1], Myung Chul Choi[2], Kwanwoo Shin[3] and Kevin Kit Parker[1]✉

Shape-memory polymeric materials lack long-range molecular order that enables more controlled and efficient actuation mechanisms. Here, we develop a hierarchical structured keratin-based system that has long-range molecular order and shape-memory properties in response to hydration. We explore the metastable reconfiguration of the keratin secondary structure, the transition from α-helix to β-sheet, as an actuation mechanism to design a high-strength shape-memory material that is biocompatible and processable through fibre spinning and three-dimensional (3D) printing. We extract keratin protofibrils from animal hair and subject them to shear stress to induce their self-organization into a nematic phase, which recapitulates the native hierarchical organization of the protein. This self-assembly process can be tuned to create materials with desired anisotropic structuring and responsiveness. Our combination of bottom-up assembly and top-down manufacturing allows for the scalable fabrication of strong and hierarchically structured shape-memory fibres and 3D-printed scaffolds with potential applications in bioengineering and smart textiles.

The growing demand of shape-memory devices in the fields of civil engineering[1], aerospace[2], wearable technology[3] and medical devices[4,5] has galvanized research beyond the conventional metal alloy archetype and towards the design of more tailorable polymeric shape-memory materials[6] with improved biocompatibility and biodegradability properties[7]. Despite the wide variety of reported systems, controlling the spatial organization of the actuation mechanisms at the molecular level through all spatial scales remains a challenge. Achieving a long-range order of the molecular actuators would lead to a much tighter control over mechanical transformation and higher-level behavioural complexity[8].

Shape-memory features have been associated traditionally with synthetic materials, but have also been observed in biological substrates as a result of the structural metastability of protein secondary structures[9]. In this regard, the keratin α-helices that are arranged in a coiled-coil architecture are known to undergo continuous structural transition into metastable β-sheets when load is applied along their longitudinal axis[10,11]. Depending on the α-keratin species, this mechanism can be either irreversible or reversible, with the latter resembling the martensitic shape-memory mechanism of metal alloys[12]. In biological tissues such as sea snail egg capsules[13] or animal skin[14], this mechanical transformation has been selected by nature to guarantee protection and to enable physiological functioning in response to external stress. This shape-memory mechanism was also observed recently in certain hair species[15].

In this work, the reversible keratin transition from α-helix to β-sheet is inspired by nature and is hypothesized to be the main mechanism for the design of a highly processable and nanostructured shape-memory material that uses hydration as trigger and is inherently biocompatible and biodegradable. Our design approach targets the recapitulation of the α-keratin hierarchical and anisotropic organization that is present in animal hair, which allows for the engineering of strong and stiff water-triggered shape-memory (WTSM) devices with tensile strength and Young's modulus that are orders of magnitude greater than those of conventional systems[16–20]. This is achieved by starting from a non-destructive extraction of keratin protofibrils from animal hair. Keratin protofibrils were found to self-organize into a nematic phase under shear stress, and their anisotropic alignment was further tuned by the charge screening effect to achieve protofibril alignment during the extrusion process. In addition to the scalable production of continuous shape-memory fibres, the material processability allowed for the use of three-dimensional (3D) printing to fabricate shape-memory architectures that are capable of complex geometrical transformations. Through the design of our keratin-based shape-memory material, we introduced the use of protein structural metastability as an actuation mechanism for the engineering of nanostructured smart materials that have long-range molecular order.

Keratin extraction and self-organization

In animal hairs, the strain-induced transition from α-helix to β-sheet is feasible because of the paired configuration of α-helices into a coiled-coil architecture (Fig. 1a)[21]. Coiled coils are hierarchically self-assembled into an anisotropic fibrillar structure that ranges from protofibrils to macrofibrils, which enables continuity of the mechanical transformation through all spatial scales. Here, fibrillar keratin was extracted from Angora wool by using lithium bromide (LiBr), a salt that can induce a reversible solid-to-liquid phase transition of crystalline keratin in water[22]. Another requirement in freeing the fibrous keratin from the hair structure is to break down the dense disulfide network of the hair matrix component. This was accomplished by using 1,4-dithiothreitol (DTT), which is capable of cleaving the disulfide bond by yielding two sulfhydryl moieties[23]. This reaction is reversible under oxidative conditions, thereby allowing for the reconstitution of the native disulfide bridges during material fabrication. Keratin was then extracted successfully by treating ground wool with an aqueous solution of LiBr and DTT at high temperature (Fig. 1b). At room temperature,

[1]Disease Biophysics Group, John A. Paulson School of Engineering and Applied Sciences, Harvard University, Cambridge, MA, USA. [2]Department of Bio and Brain Engineering, Korea Advanced Institute of Science and Technology (KAIST), Daejeon, Korea. [3]Department of Chemistry and Institute of Biological Interfaces, Sogang University, Seoul, Korea. ✉e-mail: kkparker@seas.harvard.edu

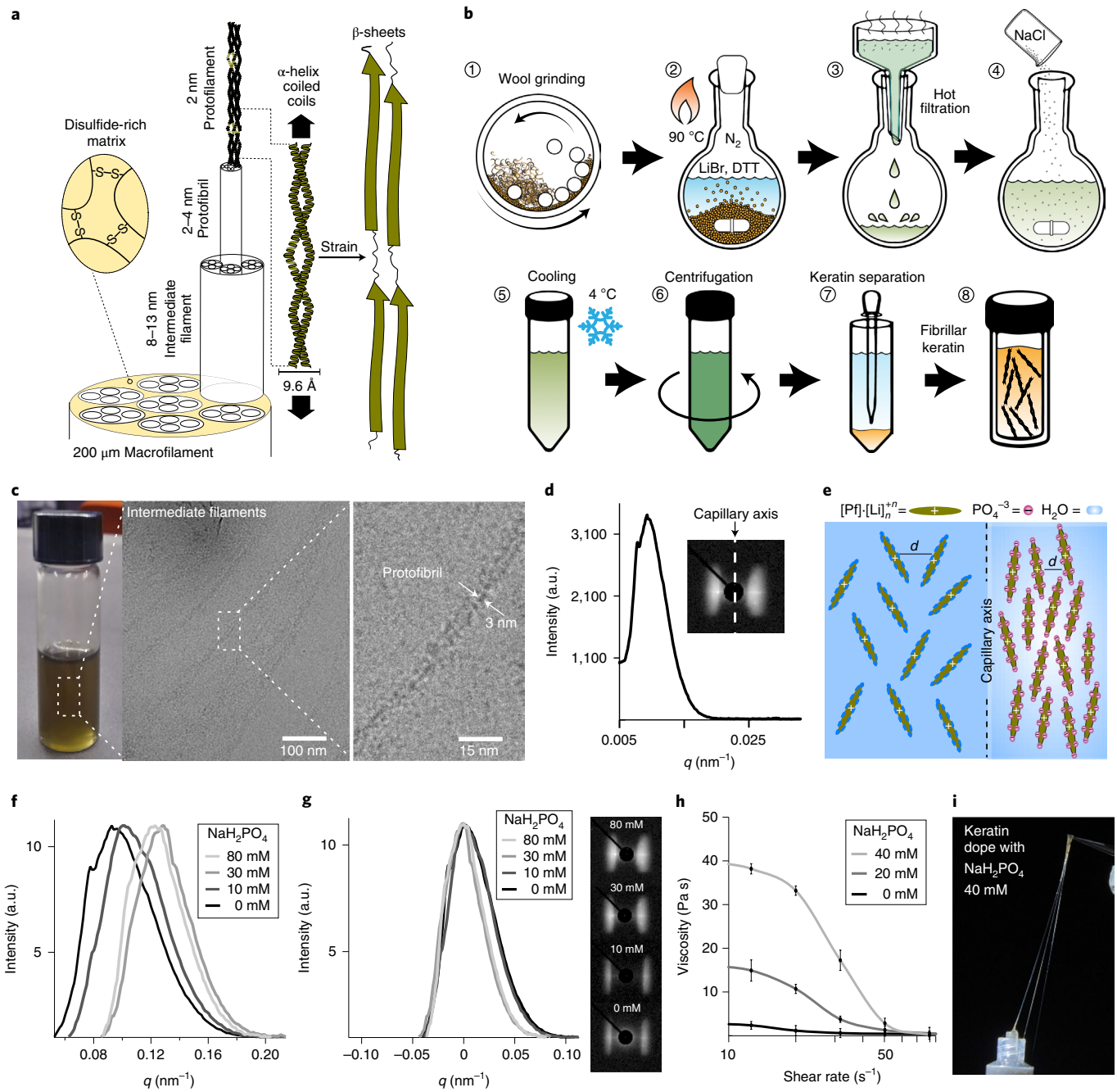

Fig. 1 | Keratin extraction protocol and nematic phase formation. a, Schematic showing the hierarchical structure of wool keratin and the transition from α-helix to β-sheet that is feasible under strain. **b**, Schematic representing the extraction protocol to obtain fibrillar keratin in solution from wool hair. **c**, Left, picture of the extracted keratin solution; centre, cryo-TEM micrograph of a keratin dope solution (×20 dilution using an 8 M LiBr aqueous solution), showing keratin intermediate filaments; right, zoomed-in cryo-TEM micrograph showing the hierarchical inner structure of intermediate filaments that are composed of protofibrils. Similar results were obtained for $n = 6$ independent cryo-TEM samples. **d**, SAXS profile of the scattering vector q for the extracted keratin solution inside a quartz capillary (1.5 mm diameter) and related 2D SAXS pattern (inset). Both indicate the nematic phase ordering of keratin under shear and spatial constraint. a.u., arbitrary units. **e**, Schematic showing the ordering of the keratin protofibrils that is triggered by the charge screening effect upon addition of NaH_2PO_4. **f**, Background-subtracted SAXS profiles of the keratin solution, showing a shift towards higher q upon addition of NaH_2PO_4 and therefore tighter packing of the keratin nematic phase. **g**, Background-subtracted SAXS profiles (left) and 2D SAXS scattering patterns (right) of the keratin solution, showing peak narrowing upon addition of NaH_2PO_4 and therefore alignment of the keratin protofilaments along the capillary axis. **h**, Rheology measurements of the keratin dope, showing an increase in viscosity and shear-thinning property upon increase in NaH_2PO_4 concentration. $n = 3$ independent batches were tested per experimental condition. Data are presented as mean values ± standard error of the mean. **i**, Picture of fibres that are drawn directly from keratin dope that contains NaH_2PO_4 at 40 mM concentration.

keratin was finally isolated through liquid–liquid phase separation, a process that was enhanced by an increase in ionic strength and further storage at low temperature. This last step of the protocol allowed for the formulation of a highly concentrated keratin solution (Supplementary Fig. 1) that had a shelf life of weeks when stored in the absence of oxygen. With its relatively high protein

content, the extracted solution is an ideal substrate for a variety of material fabrication processes. The preservation of the coiled-coil architecture of the keratin α-helices was confirmed initially by Raman spectroscopy and circular dichroism (Supplementary Figs. 2,3). This was further supported by SDS–polyacrylamide gel electrophoresis (SDS–PAGE) analysis, which showed the typical bands of the dimer and also tetramer of the coiled-coil structure (which is most likely of a heterodimeric nature, as reported for Angora wool), with very few protein degradation products (Supplementary Fig. 4).

Evidence of the keratin hierarchical structure up to the protofibrillar level was also supported by cryogenic transmission electron microscopy (cryo-TEM). Bundles were up to the micrometre range in length and had varying widths with a maximum value of approximately 10 nm (Fig. 1c), which matches the structural features of intermediate filaments[21]. Magnification of the cryo-TEM micrograph also elucidated the internal hierarchical structure of the intermediate filaments, which were composed of packed protofibrils with a consistent width of ~3 nm[21].

The recapitulation of the hierarchical architecture of keratin, which enables the long-range order of the α-helix actuation units, requires the imposition of anisotropic alignment of the protofibrils during the fabrication process. In this regard, keratin protofibrils were found to self-organize into a nematic crystal phase when subjected to shear stress and spatial constraint. This was deduced initially from the anisotropic nature of the synchrotron X-ray scattering pattern that was obtained from a sample of the keratin solution (401.7 mg ml^{-1}) prepared in a quartz capillary (Fig. 1d) (ref. [24]). During the analysis, the capillary was placed perpendicular to the X-ray beam and with its longitudinal axis parallel to the meridian axis of the detector. The equatorial nature of the scattering pattern suggests that the keratin domains were preferentially oriented parallel to the capillary axis (Fig. 1d, inset). The average distance among the keratin domains is associated with the lattice size parameter d, which is obtained from the maximal intensity of the scattering vector modulus q as defined by $d = 2\pi/q$ (ref. [24]). The nematic ordering of the keratin protofilament is reasoned to be the result of the shear stress that is generated at the capillary wall during sample preparation and of the further stabilization by the space constraint[24]. In this scenario, enhancement in stiffness and self-assembly of the keratin protofibrils is expected to lead to a higher degree of order of the nematic phase. Therefore, tighter control over the self-organization of the keratin liquid crystal phase was achieved by promoting protein–protein interactions through the charge screening effect[25]. Owing to the presence of lithium cations that are absorbed on the protein surface, keratin is expected to have a net positive charge[26]. The phosphate anion is known to have a high screening effect towards positively charged surfaces[25] and was therefore used for this purpose (Fig. 1e). The addition of sodium dihydrogen phosphate (NaH_2PO_4) indeed caused tightening of the keratin nematic phase packing, which is indicated by a peak shift towards a higher value of q (Fig. 1f). Upon addition of the kosmotropic salt, narrowing of the equatorial scattering pattern and consequent sharpening of the scattering peak were also observed, which indicate an increase in the keratin domain alignment along the capillary axis (Fig. 1g).

The tuning of the keratin nematic phase organization through protein charge screening dramatically affects the rheological properties of the protein solution. Upon increase in NaH_2PO_4, aggregation of the protofibrils causes enhancement of the protein solution viscosity at low shear rates (Fig. 1h) (ref. [27]). This finding is in agreement with small-angle X-ray scattering (SAXS) data, which show a tighter packing of the keratin filaments upon addition of the kosmotropic salt. However, upon increase in shear rate, the alignment of the keratin protofibrils causes a sudden decrease in viscosity, which confers a pronounced shear-thinning behaviour to the protein solution. The presence of steeper slopes upon increase in NaH_2PO_4 further supports a higher degree of alignment of the keratin protofibrils, which is induced by the stiffening of crystallized proteins. With a NaH_2PO_4 concentration of 40 mM and protofilament concentration of 401.7 mg ml^{-1}, the keratin dope shows viscoelastic properties that are suitable in further processing, as fibres could be formed directly simply by pulling the protein with tweezers (Fig. 1i). Upon decrease in NaH_2PO_4 concentration, the keratin solution loses its viscoelastic properties, and fails to form fibres directly from the solution (Supplementary Fig. 5).

Hierachical structuring and anisotropy in keratin fibres

The alignment of the keratin α-helices along the fibre axis is a design criterion to ensure high strength and high fixity yields of the fibres. When the α-helix axes are parallel to the pulling vector, the maximum uncoiling of α-helices can be obtained, thereby enabling a greater material strain to failure owing to plastic deformation and reorganization. To this point, the ability of the keratin protofibrils to self-organize into a nematic phase is ideal for fabricating hierarchically structured shape-memory materials through extrusion processes. Therefore, anisotropic keratin fibres could be spun by using a traditional wet-spinning platform. An aqueous solution of NaH_2PO_4 is used as antisolvent, which allows for both the outer diffusion of LiBr from the extruded keratin dope and further self-assembly of the protein through the charge screening effect (Fig. 2a and Supplementary Fig. 6). The restoration of the disulfide covalent network was enabled by the oxidative activity of hydrogen peroxide (H_2O_2) on the cysteine thiol group[28]. The high protein concentration in the dope conferred robustness to the fibre during the coagulation process, which allowed for a flexible and reliable spinning process. Continuous and homogeneous fibres could be produced (Fig. 2b) and high drawing rates could be applied, thereby enabling fibre diameters of 10 μm (Supplementary Fig. 7).

The nematic phase organization of the keratin protofibrils leads to a fibrillation process that generates hierarchically structured and anisotropic fibres. Scanning electron microscopy (SEM) shows how a single fibre is composed of continuous fibrils that are at least a few tens of micrometres long (Fig. 2b). The cross-sectional area confirms that the fibrils are in the 50 nm range in diameter and constitute the core of the fibre (Fig. 2d). Polarized optical microscopy supports the anisotropic nature of the fibre core by showing its birefringence behaviour with a maximum of the transmitted light intensity at 45° (Fig. 2e). The orientation of the α-helices along the fibre axis was confirmed by polarized Raman spectroscopy, which shows the highest intensities for the amide I signal (C=O stretching mode) when the fibre is oriented parallel to the laser, for both the cross and non-cross combinations of the laser and the analyser (Fig. 2f) (ref. [29]).

Insights into the coiled-coil structure and anisotropic organization were obtained through wide-angle X-ray scattering (WAXS) analysis. The two-dimensional (2D) scattering profile shows the characteristic equatorial reflection at 9.65 Å, which corresponds to the spacing between the axes of adjacent α-helices (Fig. 2g) (ref. [30]). The one-dimensional (1D) analysis along the meridian axis shows the presence of the characteristic meridian and off-meridian reflections that correspond to the α-helix pitch projection and were detected at 5.15 Å (shoulder) and 5.05 Å (maximum), respectively (Fig. 2h and Supplementary Fig. 8) (ref. [31]). However, compared to results for the Angora wool fibre, these reflections are broader and have a different reciprocal intensity ratio, which suggests that the α-helices are less crystalline than the natural analogue (Supplementary Fig. 8). Furthermore, the scattering arc in the 5 Å equatorial region indicates that some of the α-helices are more randomly oriented (Fig. 2h). In addition, the fact that the maximum is shifted towards higher q values suggests the presence of uncoiled peptide chains, which are oriented parallel to the fibre axis and most likely arranged into a β-sheet conformation (Fig. 2i) (ref. [30]). The uncoiling of peptide chains is hypothesized to be caused by the

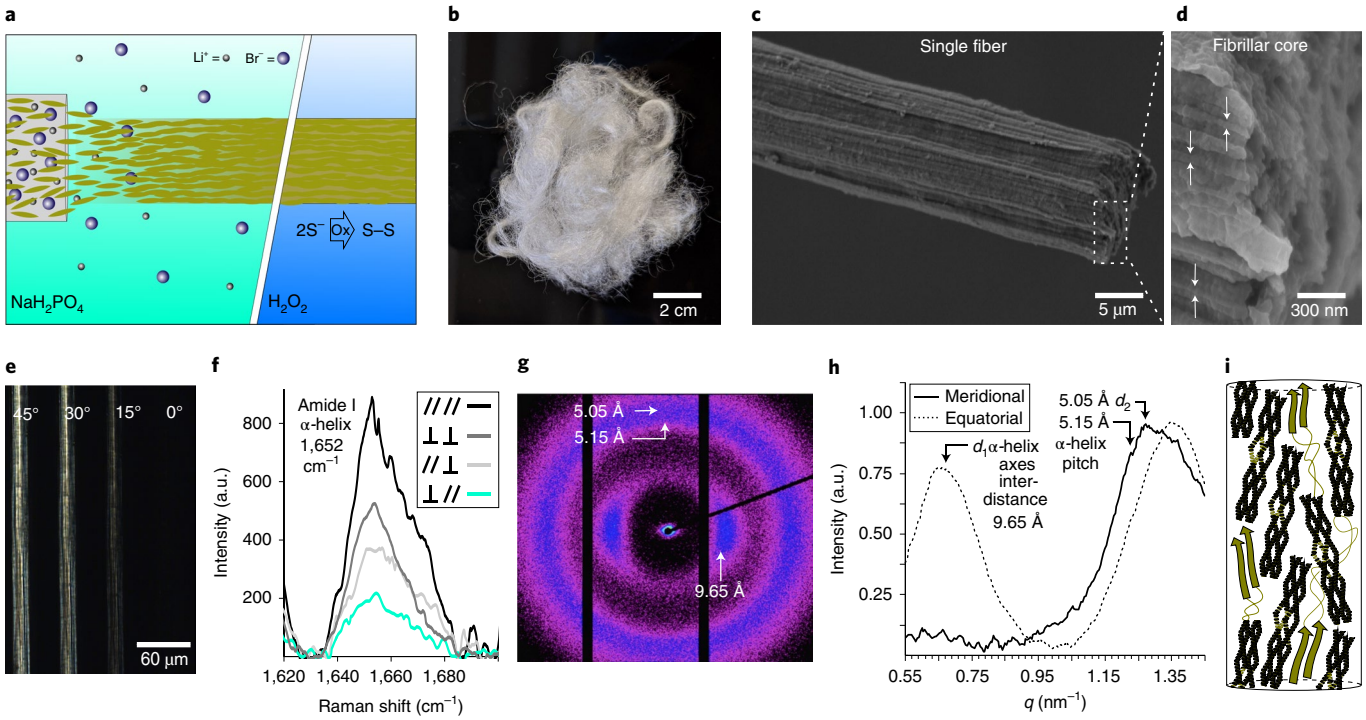

Fig. 2 | Keratin fibre spinning and structural characterization. a, Schematic representing the transition from the keratin nematic phase to the anisotropic fibre. **b**, Picture of a continuous keratin fibre approximately 100 m in length. **c**, SEM micrograph of a keratin fibre, showing its fibrillar structure. Similar results were obtained for $n = 6$ independent SEM samples. **d**, Zoom-in of both edge and cross-section of the fibre, showing the fibrillar structure of the fibre core. **e**, Polarized light microscopy image showing the anisotropic birefringence of the fibre. Similar results were obtained for $n = 3$ independent fibre samples. **f**, Polarized Raman spectroscopy in the amide I region (1,620–1,700 cm^{-1}) of a single keratin fibre that is oriented parallel to both laser and analyser (black), perpendicular to both laser and analyser (grey), parallel to the laser and perpendicular to the analyser (light grey) and perpendicular to the laser and parallel to the analyser (light blue). **g**, 2D WAXS scattering pattern obtained from a bundle of keratin fibres that are oriented perpendicular to the X-ray beam and parallel to the meridian axis of the detector, with white arrows pointing to the meridional and equatorial reflections. The black bars are non-detecting areas that correspond to the gaps between the detector plates. **h**, 1D WAXS scattering profiles showing a maximum at 5.05 Å and a shoulder at 5.15 Å that correspond to the α-helix pitch projections (meridional), and a maximum at 9.65 Å that corresponds to the spacing between adjacent α-helix axes (equatorial). **i**, Schematic of the fibre structure composed of coiled coils that are aligned along the fibre axis. A fraction of α-helices is denaturated into uncoiled peptide chains and β-sheets during fibre spinning.

tensile stress that is generated during fibre spinning, which leads to a partial denaturation of the coiled-coil anisotropic architecture.

Hydration-responsive shape-memory fibres

The shape-memory effect of the designed keratin fibres relies on the reversible uncoiling of the α-helix and on the formation of metastable β-sheets when uniaxial strain is applied (Fig. 3a), a concept that was pioneered by Miserez et al.[13]. Tensile tests that were carried out on single keratin fibres confirm this mechanism by showing an initial elastic behaviour up to ~5% strain (Young's modulus of 4.18 ± 0.10 GPa) followed by a yielding region that is characterized by a constant yield stress (96.1 ± 3.1 MPa) (Fig. 3b); this response corresponds to the α-helix unfolding process. As the strain increases further, the uncoiled and elongated keratin peptide chains are stabilized in their stretched geometry by assembling into β-sheets (Fig. 3c). This β-sheet-forming region is characterized by a strain hardening at ~50% strain, as the applied load is not only dissipated by the disruption of the coiled coils but also carried by the stretching of the β-sheets. As load is removed at 100% strain (tensile strength of 137.18 ± 1.03 MPa), the fibre shows a plastic strain (~85%) that is in agreement with the entrapment of the keratin unfolded chains into the new metastable β-sheets. Overall, the mechanical properties of the designed keratin fibres match those of native wool hair[32]. The rearrangement of the protein secondary structure during this strain-induced transition from α-helix to β-sheet was monitored by tracking the shift of the amide I Raman signal, which is known to have two distinct scattering bands, at 1,652 cm^{-1} for the α-helix and at 1,671 cm^{-1} for the β-sheet[33]. A small fraction of β-sheets is already present in the unstrained fibre (Fig. 3d), which is in agreement with the WAXS data already provided. At 100% strain, a blue shift of the amide I band is observed, and integration of the deconvoluted peaks clearly suggests the increase in the β-sheets component upon conversion of the coiled-coil α-helices. The strain-induced transition from α-helix to β-sheet was also supported by WAXS analysis, which shows the formation of the characteristic 4.65 Å equatorial reflection that corresponds to the lateral distances between the peptide chains in a β-sheet secondary structure (Fig. 3e) (ref. [30]). Uncoiling of the α-helices is indicated by the decrease in intensity of the meridian reflections in the 2D pattern, and by the 5.05 Å and 5.15 Å maxima shifts towards higher values of q in the 1D meridian scattering profile (Supplementary Fig. 9). The fact that the equatorial signal in the 9 Å region is almost unshifted suggests that the β-sheet structures preserve the spacing of the α-helices and therefore originate from the coiled-coil architectures. The change in the WAXS 2D pattern is in agreement with the mechanism of the transition from α-helix to β-sheet that occurs in natural fibres.

In the stretched fibre, β-sheets are kinetically stable owing to the presence of the hydrogen bond network that hinders their

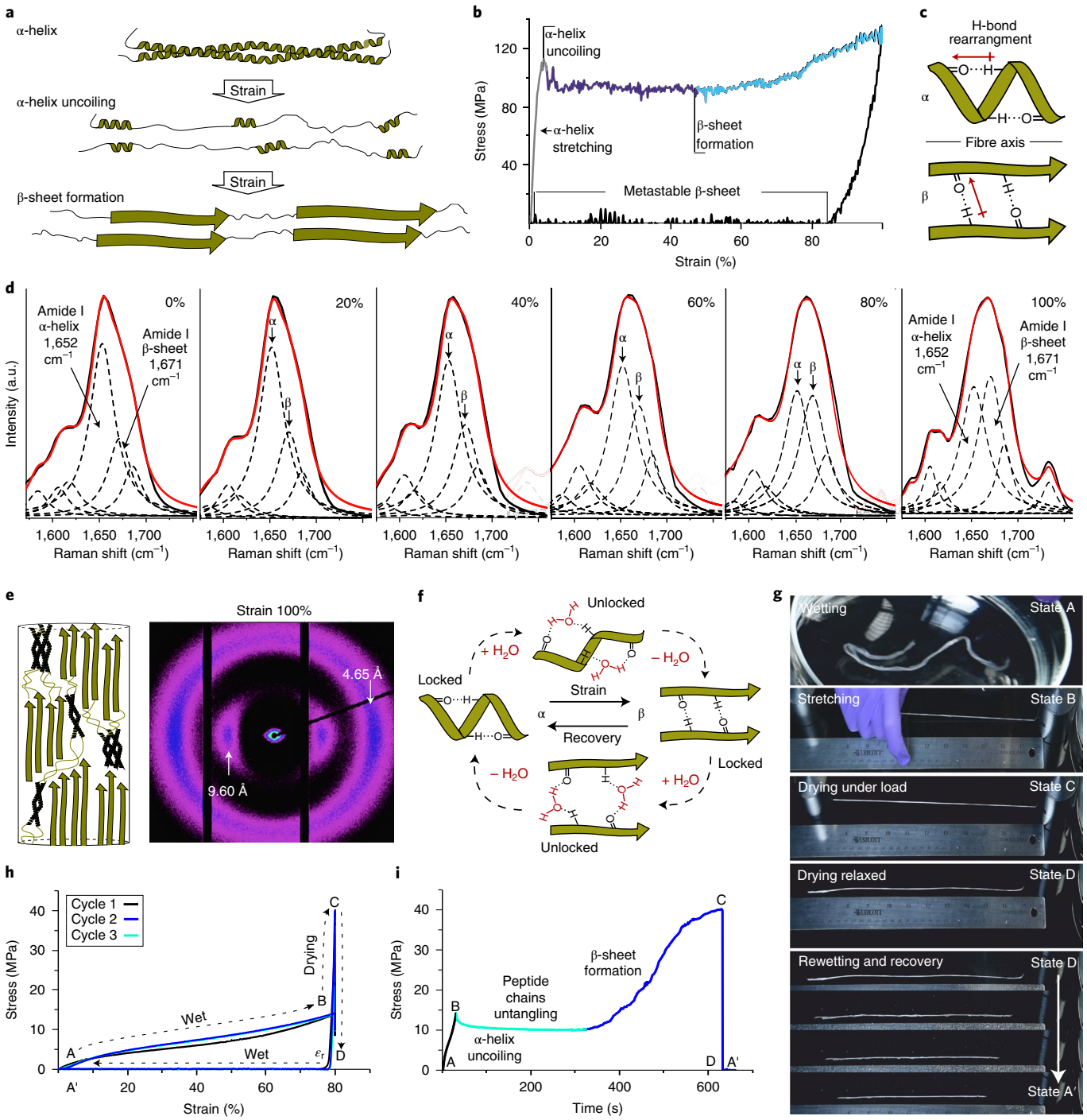

Fig. 3 | Shape-memory effect in keratin fibres. a, Schematic of the keratin protein secondary structure rearrangement during the transition from α-helix to β-sheet under strain. **b**, Stress–strain plot of a single keratin fibre (representative of $n = 3$ curves), showing the three typical regions in the transition from α-helix to β-sheet as function of strain: initial elastic behaviour (grey), yielding (blue) and sheet assembly (cyan). **c**, Schematic showing the hydrogen bond network that is responsible for the formation of the keratin secondary structures, and the change in the bond orientation within the fibre as keratin rearranges from the α structure to the β structure. **d**, Strain-dependent Raman spectroscopy of a single keratin fibre. The black and red solid lines represent the experimental peak and the sum of the calculated peaks, respectively, whereas the dashed lines correspond to the single calculated peaks. **e**, Schematic showing the formation of β-sheets from coiled coils and their alignment along the fibre axis (left). 2D WAXS pattern of the strained fibre, with white arrows pointing to the characteristic equatorial reflections (right). **f**, Schematic representing the WTSM mechanism. **g**, Screenshots taken from Supplementary Video 1 and illustrating the WTSM behaviour of the keratin fibre bundle. States of the yarn during the process: A, wet and relaxed; B, wet under load; C, dry under load; D, dry and relaxed after stretch; A', wet and relaxed after recovery. **h**, Stress–strain plot of a keratin fibre yarn that undergoes multiple water-triggered shape transitions. **i**, Stress–time plot of the full cycle 2 from the plot in **h**. Panel **a** adapted with permission from ref. [13], Springer Nature Ltd.

reconversion into the more thermodynamically stable α-helices. With leveraging of this property, a shape-memory cycle can therefore be elaborated in which the hydrogen bonding network functions as a locking mechanism to ensure the fixity of the deformed shape. Here, water is used as a stimulus to facilitate both fibre deformation and recovery to the original shape (Fig. 3f). This

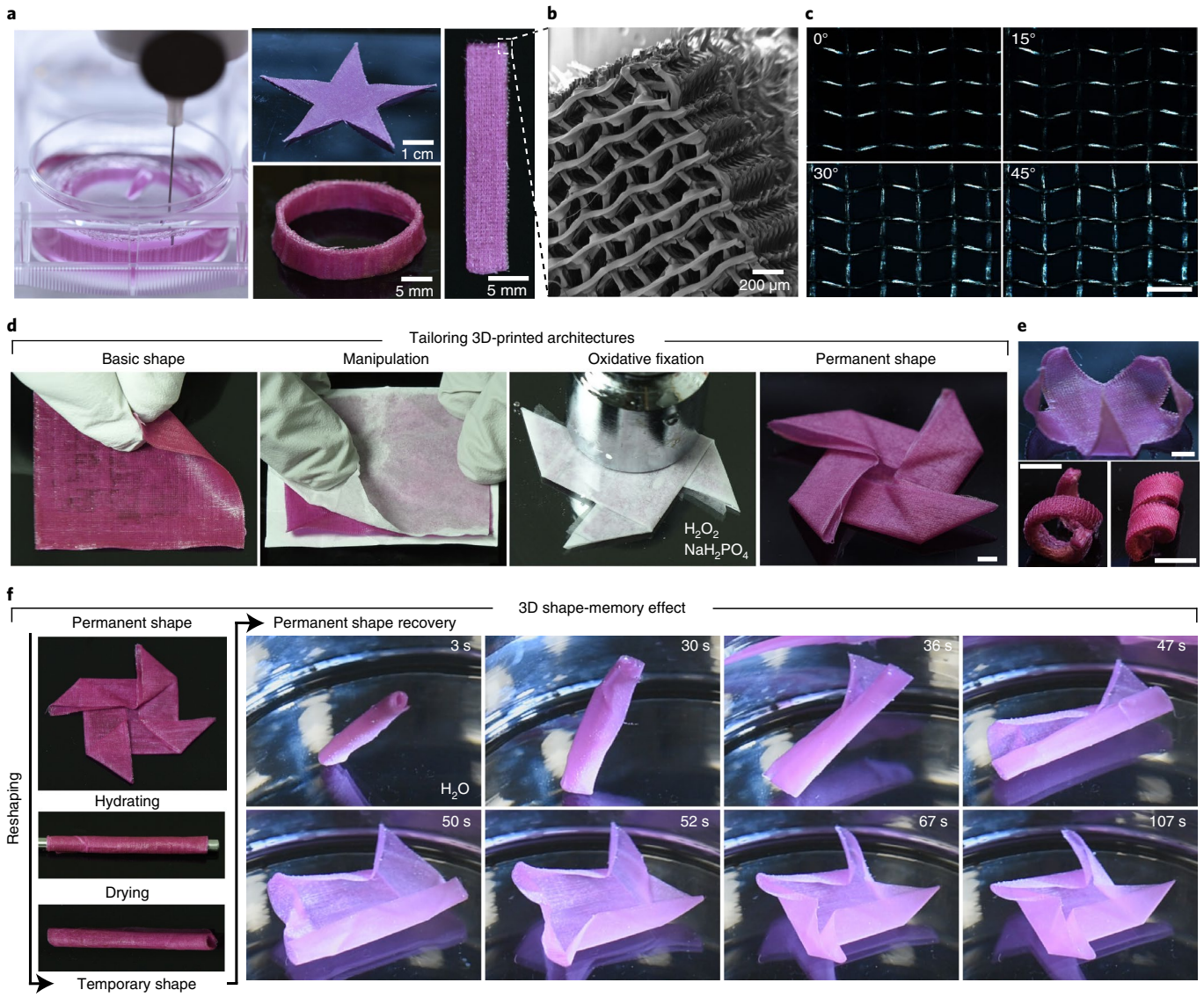

Fig. 4 | Shape-memory effect in 3D-printed architectures. a, Photograph illustrating the 3D printing process that uses the extracted keratin as an ink (401.7 mg ml^{-1}, 40 mM NaH_2PO_4) and a pluronic solution (25% v/w) as both a supporting and coagulation bath (left). Images of basic 3D-printed keratin architectures such as flat star, ring and flat strip (right). For image clarity, the keratin solution was dyed with Rhodamine B to give the objects a magenta colour. **b**, SEM micrographs showing the 3D structure of the keratin architecture that is composed of aligned and stacked fibres deposited in a rectilinear pattern. Similar results were obtained for $n = 4$ independent SEM samples. **c**, Polarized light microscopy images of a rectilinear 3D-printed pattern showing the anisotropic birefringence for aligned single fibres. Similar results were obtained for $n = 3$ independent 3D-printed grids. Scale bar, 400 µm. **d**, Sequence of photographs illustrating the post-3D-printing process that is implemented to tailor the shape of basic 3D-printed structures. Specifically, a star-shaped origami model is obtained from a flat square, which is first sandwiched between two paper sheets, then folded into the desired origami architecture, and finally fixed in a H_2O_2 and NaH_2PO_4 aqueous solution. Scale bar, 5 mm. **e**, Photographs of a star with bent arms (top) and of spirals (bottom) that were obtained by post-3D-printing processing. Scale bars, 1 cm. **f**, Photographs showing the WTSM effect in 3D architectures, which is illustrated with a star-shaped origami model.

concept was tested for a bundle of keratin fibres of same diameter (Fig. 3g and Supplementary Video 1). The fibre bundle was hydrated in deionized water for a few seconds (state A), stretched manually in the air while still in a wet state (state B) and then kept under load at room temperature for 10 min to let the fibres dry (state C). When weights were removed to allow the fibre bundle to relax, no visible or noticeable change in length between the stretched and relaxed forms was observed (state D). The ability of the bundle to recover its original length was then confirmed by applying nebulized deionized water, which triggered the shrinking of the fibres back to their original length within a few seconds (state A'). When compared to the experiment conducted in the dry state (Fig. 3b), tensile tests clearly showed the role of water in facilitating the protein structure rearrangement. This is indicated by an overall decrease in tensile stress (Fig. 3h) and a more gradual transition among the elastic, yielding and post-yielding regions. As the fibre dries under load, the formation of β-sheets is indicated by a sudden increase in stress that corresponds to a stiffening of the fibres, which can be measured over time as the fibres dehydrate and hydrogen bonds form (Fig. 3i). When the load is released, the fibres retain their stretched form with a ~94% fixity yield (R_f), which is calculated as the ratio between the total

strain applied ($\varepsilon_{tot} = 80\%$) and the residual strain ($\varepsilon_r \cong 77\%$). After rehydration, the recovery efficiency of the fibres reached values close to 100%, which was confirmed after additional stress–strain cycles (Fig. 3h).

Owing to the long-range order of its hierarchical fibrillar structure, the engineered shape-memory material, in its dry state, has a tensile strength (137.18 ± 1.03 MPa) and a Young's modulus (4.18 ± 0.10 GPa) one order and two orders of magnitude higher, respectively, than those of other reported WTSM materials (Supplementary Table 1 and Supplementary Fig. 10). These values are of the same order of magnitude as those of Nylon 6,6 and worm silk fibres[34,35]. The engineered material tensile strength of 14.94 ± 0.46 MPa upon hydration is still one order of magnitude higher than that of the reported WTSM materials, and of the same order of magnitude as tensile strengths of polyurethane elastomers that are used in the textile industry[36].

The role of the anisotropic organization of the protofibrils in conferring such high mechanical properties to the keratin fibres was supported by comparison with isotropic thin films that were obtained from the same extracted keratin solution (Supplementary Fig. 11). The films showed a dramatic decrease in tensile strength (greater than an order of magnitude) and in strain to failure (two orders of magnitude), with no plastic deformation attributed to the transition from α-helix to β-sheet.

3D printing of hydration-responsive shape-memory architectures

The processability of the keratin dope was further extended to 3D printing technology for the fabrication of more complex shape-memory architectures that featured one-way shape-memory modality. Basic geometries could be fabricated by extruding the protein dope into a hydrogel[37] that served as both a supporting and coagulation bath (Fig. 4a). The shear-thinning properties of the dope allowed for the use of small-diameter extrusion needles, which enabled the production of 3D-printed volumes with small textural features on a scale of approximately 50 μm (Fig. 4b). As shown by the birefringence patterns that were obtained from polarized light microscopy, the alignment of the keratin protofibrils follows the 3D printing extrusion pathway, and therefore leads to highly ordered architectures that feature an inherent structural hierarchy that spans from molecular to macroscopic levels (Fig. 4c).

After the 3D printing process, fixation of the permanent shape requires the formation of disulfide bridges through H_2O_2-induced oxidation. However, before this oxidative step, the 3D-printed objects are mechanically stable without the supporting bath, and therefore can be manipulated plastically. A star-shaped origami model was fabricated by manually folding a 3D-printed squared sheet and permanently fixing its new configuration in a solution of H_2O_2 and NaH_2PO_4 (Fig. 4d). This two-step fabrication process allows for the tailoring of 3D-printed basic geometries to achieve permanent architectures with a higher degree of complexity (Fig. 4e).

As with the wet-spun fibres, the 3D-printed objects have moisture-responsive shape-memory properties. The star-shaped origami architecture was chosen to illustrate the efficiency of the shape-memory mechanism in operating rather sophisticated geometrical transformations. When hydrated, the 3D-printed origami model is malleable and can be unfolded and arbitrarily reshaped as a rolled tube, for instance (Fig. 4f, left). As it dries, the square sheet loses its malleability and is locked in its new temporary shape. Recovery of the star-shaped origami architecture is then triggered by rehydration, a process that occurs over a time scale of only seconds because of the high surface-to-volume ratio that causes quick exposure of the bulk keratin to the water (Fig. 4f, right). To regain the original origami shape, the square sheet first opens up through an unrolling process and then correctly refolds through a cooperative bending process of the edges.

Overall, we have developed a hierarchically structured fibre that is based on fibrillar keratin and that therefore possesses unique shape-memory properties and high mechanical stability. By using a two-stage 3D printing process in which we first allow the proteins to coagulate and then cross-link them through an oxidative treatment, we can print fibres into complex shape-memory textile materials. This new material, which can be resourced in a sustainable manner, will enable the manufacturing of biodegradable smart textiles such as body-adaptable garments or gears that absorb strain energy.

Outlook

Here, we propose a bioinspired design for the fabrication of a biocompatible and hierarchically structured shape-memory material from waste keratin. The unique combination of high mechanical performances and shape-memory effect makes the engineered material suitable for the design of actuators that find application in the smart textile industry. The biocompatibility and body affinity of the material can be leveraged to replace oil-based polymers for the engineering of strain-responsive and body-adaptable apparel. The processability of the material through additive manufacturing platforms allows for the production of complex architectures with structural features in the micrometre range, which makes the material suitable for a vast range of bioengineering applications.

Online content

Any methods, additional references, Nature Research reporting summaries, source data, extended data, supplementary information, acknowledgements, peer review information; details of author contributions and competing interests; and statements of data and code availability are available at https://doi.org/10.1038/s41563-020-0789-2.

Received: 13 September 2019; Accepted: 29 July 2020;
Published online: 31 August 2020

References

1. Cladera, A. et al. Iron-based shape memory alloys for civil engineering structures: an overview. *Constr. Build. Mater.* **63**, 281–293 (2014).
2. L. Santo, L., Quadrini, F., Accettura, A. & Villadei, W. Shape memory composites for self-deployable structures in aerospace applications. *Procedia Eng.* **88**, 42–47 (2014).
3. Hu, J., Meng, H., Li, G. & Ibekwe, S. I. A review of stimuli-responsive polymers for smart textile applications. *Smart Mater. Struct.* **21**, 053001 (2012).
4. Opie, N. L. et al. Focal stimulation of the sheep motor cortex with a chronically implanted minimally invasive electrode array mounted on an endovascular stent. *Nat. Biomed. Eng.* **2**, 907–914 (2018).
5. Montgomery, M. et al. Flexible shape-memory scaffold for minimally invasive delivery of functional tissues. *Nat. Mater.* **16**, 1038–1046 (2017).
6. Liu, C., Qin, H. & Mather, P. T. Review of progress in shape-memory polymers. *J. Mater. Chem.* **17**, 1543–1558 (2007).
7. Peterson, G. I., Dobrynin, A. V. & Becker, M. L. Biodegradable shape memory polymers in medicine. *Adv. Healthc. Mater.* **6**, 1700694 (2017).
8. Lendlein, A. & Gould, O. E. C. Reprogrammable recovery and actuation behaviour of shape-memory polymers. *Nat. Rev. Mater.* **4**, 116–133 (2019).
9. Fischer, F. D., Harrington, M. J. & Fratzl, P. Thermodynamic modeling of a phase transformation in protein filaments with mechanical function. *New J. Phys.* **15**, 065004 (2013).
10. Fudge, D. S., Gardner, K. H., Forsyth, V. T., Riekel, C. & Gosline, J. M. The mechanical properties of hydrated intermediate filaments: insights from hagfish slime threads. *Biophys. J.* **85**, 2015–2027 (2003).
11. Miserez, A. & Guerette, P. A. Phase transition-induced elasticity of α-helical bioelastomeric fibres and networks. *Chem. Soc. Rev.* **42**, 1973–1995 2013).
12. Falk, W. & James, R. D. Elasticity theory for self-assembled protein lattices with application to the martensitic phase transition in bacteriophage T4 tail sheath. *Phy. Rev. E* **73**, 011917 (2006).
13. Miserez, A., Wasko, S. S., Carpenter, C. F. & Waite, J. H. Non-entropic and reversible long-range deformation of an encapsulating bioelastomer. *Nat. Mater.* **8**, 910–916 (2009).
14. Latorre, E. et al. Active superelasticity in three-dimensional epithelia of controlled shape. *Nature* **563**, 203–208 (2018).

15. Xiao, X. & Hu, J. Animal hairs as water-stimulated shape memory materials: mechanism and structural networks in molecular assemblies. *Sci. Rep.* **6**, 26393 (2016).
16. Tian, T. et al. A body temperature and water-induced shape memory hydrogel with excellent mechanical properties. *Polym. Chem.* **10**, 3488–3496 (2019).
17. Alavijeh, R. Z., Shokrollahi, P. & Barzin, J. A thermally and water activated shape memory gelatin physical hydrogel, with a gel point above the physiological temperature, for biomedical applications. *J. Mater. Chem. B* **5**, 2302–2314 (2017).
18. Gu, X. & Mather, P. T. Water-triggered shape memory of multiblock thermoplastic polyurethanes (TPUs). *RSC Adv.* **3**, 15783–15791 (2013).
19. Khoury, L. R. & Popa, I. Chemical unfolding of protein domains induces shape change in programmed protein hydrogels. *Nat. Commun.* **10**, 5439 (2019).
20. Guo, Y. et al. A biodegradable functional water-responsive shape memory polymer for biomedical applications. *J. Mater. Chem. B* **7**, 123–132 (2019).
21. Popescu, C. & Höcker, H. Hair—the most sophisticated biological composite material. *Chem. Soc. Rev.* **36**, 1282–1291 (2007).
22. Mandelkern, L., Halpin, J. C., Diorio, A. F. & Posner, A. S. Dimensional changes in fibrous macromolecules: the system α-keratin-lithium bromide. *J. Am. Chem. Soc.* **84**, 1383–1391 (1962).
23. Whitesides, G. M., Lilburn, J. E. & Szajewski, R. P. Rates of thiol-disulfide interchange reactions between mono- and dithiols and Ellman's reagent. *J. Org. Chem.* **42**, 332–338 (1977).
24. Davidson, P., Penisson, C., Constantin, D. & Gabriel, J.-C. P. Isotropic, nematic, and lamellar phases in colloidal suspensions of nanosheets. *Proc. Natl Acad. Sci. USA* **15**, 6662–6667 (2018).
25. Schwierz, N., Horinek, D. & Netz, R. R. Anionic and cationic Hofmeister effects on hydrophobic and hydrophilic surfaces. *Langmuir* **29**, 2602–2614 (2013).
26. Bello, J. & Bello, H. R. Interaction of model peptides with water and lithium bromide. *Nature* **190**, 440–441 (1961).
27. Abitbol, T., Kam, D., Levi-Kalisman, Y., Gray, D. G. & Shoseyov, O. Surface charge influence on the phase separation and viscosity of cellulose nanocrystals. *Langmuir* **34**, 3925–3933 (2018).
28. Luo, D., Scott, S. W. & Anderson, B. D. Kinetics and mechanism of the reaction of cysteine and hydrogen peroxide in aqueous solution. *J. Pharm. Sci.* **94**, 304–316 (2005).
29. Rintoul, L., Carter, E. A., Stewart, S. D. & Fredericks, P. M. Keratin orientation in wool and feathers by polarized Raman spectroscopy. *Biopolymers* **57**, 19–28 (2000).
30. Kreplak, L., Doucet, J., Dumas, P. & Briki, F. New aspects of the α-helix to β-sheet transition in stretched hard α-keratin fibers. *Biophys. J.* **87**, 640–647 (2004).
31. Busson, B., Briki, F. & Doucet, J. Side-chains configurations in coiled coils revealed by the 5.15-Å meridional reflection on hard α-keratin X-ray diffraction patterns. *J. Struct. Biol.* **125**, 1–10 (1999).
32. Kim, J.-H. et al. Review of nanocellulose for sustainable future materials. *Int. J. of Precis. Eng. and Manuf.–Green Tech.* **2**, 197–213 (2015).
33. Paquin, R. & Colomban, P. Nanomechanics of single keratin fibres: a Raman study of the α-helix→β-sheet transition and the effect of water. *J. Raman Spectrosc.* **38**, 504–514 (2007).
34. Adams, W. W. & Eby, R. K. High-performance polymer fibers. *MRS Bull.* **12**, 22–26 (1987).
35. Guo, C. et al. Structural comparison of various silkworm silks: an insight into the structure–property relationship. *Biomacromolecules* **19**, 906–917 (2018).
36. Pang, B. et al. Design and preparation of a new polyurea-polysiloxane–polyether copolymer with a block soft segment prepared by utilizing aza-Michael addition reaction. *Polym. Chem.* **9**, 869–877 (2018).
37. Kolesky, D. B. et al. 3D bioprinting of vascularized, heterogeneous cell-laden tissue constructs. *Adv. Mater.* **26**, 3124–3130 (2014).

Publisher's note Springer Nature remains neutral with regard to jurisdictional claims in published maps and institutional affiliations.

© The Author(s), under exclusive licence to Springer Nature Limited 2020

Methods

General methods. All reagents were commercially available and used without further purification unless otherwise stated. Angora wool was purchased from the R. H. Lindsay Wool Company. LiBr, H_2O_2, NaH_2PO_4, Rhodamine B and DTT were obtained from Sigma Aldrich, and Pluronic F127 Prill surfactant was purchased from BASF. Slide-A-Lyzer dialysis cassettes with a cut-off of 3.5 kDa and 0.1–0.5 ml capacity were purchased from Thermo Fischer Scientific. Ultraviolet–visible spectra were recorded with an Agilent Cary 60 UV–Vis spectrophotometer and a 1 cm path quartz cuvette, and data collection and analysis were carried out with Cary WinUV v.2 software. Raman spectroscopy was performed with an Horiba XploRA PLUS hyperspectral darkfield Raman microscope that used a 785 nm excitation laser, whereas polarized Raman spectra were recorded with a Horiba LabRAM HR Evolution Raman microscope that used a 633 nm excitation laser. Raman spectroscopy data collection and analysis were carried out with LabSpec v.6.4.4 software. Rheology measurements were performed with an Ares-G2 rheometer that had a conical geometry 40 mm in diameter, and data collection and analysis were carried out with TRIOS v.4.4.1 software (TA instruments). Circular dichroism spectra were recorded with a JASCO J-815 circular dichroism spectrometer and a 0.5 cm path quartz cuvette, and data collection and analysis were carried out with Spectra Manager v.2 software.

Wool grinding protocol. First, the wool was washed with ethanol for 40 h by using a Soxhlet continuous extraction system, rinsed with water and allowed to dry at room temperature (21 °C). Subsequently, wool fibres were cut manually into shorter segments (approximately 5 mm in length) and ground to micrometre-sized particles with a Retsch PM 100 planetary ball mill. A 20.5 g quantity of cut wool was placed in a 250 ml stainless steel jar together with stainless steel balls (90 ml, 5 mm in diameter) and ground at 450 r.p.m. for 3 h in intervals of 5 min every 20 min.

Keratin extraction protocol. In a N_2 atmosphere, wool powder (9.5 g) was suspended in an aqueous solution (150 ml) of LiBr (8 M) and DTT (0.100 mM), and the solution was stirred vigorously at 90 °C for 36 h. Afterwards, wool residue was collected by hot filtration under negative pressure and the solution was allowed to cool to room temperature. NaCl (2.30 g, 25 g ml^{-1}) was added portion-wise while the solution was stirred, and the solution was then stored at 4 °C for 12 h to obtain a heavy keratin colloidal phase through phase separation. The colloidal protein phase that formed was separated from the solution through centrifugation (3,000 r.p.m., 4 °C) and collected as a yellowish viscous liquid (10.31 ml). The obtained keratin solution was dialysed against water (3 × 2 l) over two days by using a dialysis cassette with a 3.5 kDa cut-off, and finally freeze-dried to obtain a white solid. Based on a Bradford assay, the extracted keratin solution concentration was calculated to be 401.7 ± 15 mg ml^{-1} (total yield of 43.6%).

Scanning electron microscopy. Samples were deposited on an SEM stub (12.5 mm in diameter) that was covered with carbon tape and then sputter-coated with Pt/Pd (10 nm thickness) with an EMS 200T D dual-head sputter coater. SEM micrographs were taken with a Zeiss Ultra Plus field emission scanning electron microscope that used an electric high tension of 2 kV and an SE2 detector. Data collection and analysis were carried out with SmartSEM v.05.06 image processing software.

3D printing. A Cellink BIO X 3D printer was used as 3D printing platform. The keratin dope was extruded at 40 °C under an absolute pressure of 90 kPa and through a 36 gauge needle that was moving at a speed of 8 mm s^{-1}. A Pluronic F127 (25% m/v) aqueous solution was used as both coagulating and supporting baths. To help visualize the object structure during printing, Rhodamin B was added to the keratin dope as magenta-coloured tracer. After 3D printing, the Pluronic F127 was removed by washing with a cold (~0 °C) 0.4 M NaH_2PO_4 solution. Oxidative fixation was carried out with a H_2O_2 (1% v/v) aqueous solution for 1 h.

Cryo-transmission electron microscopy. For cryo-TEM analysis, a droplet (5 µl) of the sample solution was placed on a Quantifoil 'holey' R2/1 grid (with copper) that had been hydrophilized through plasma treatment. The excess fluid was blotted to create an ultra-thin layer (typical thickness of 200–300 nm) of the solution, which spanned the holes of the support film. The prepared samples were vitrified by quick immersion of the grids into liquid ethane at its freezing point (−184 °C) by using a Gatan Cryoplunge 3 system. The vitrified sample grids were transferred under liquid nitrogen into an FEI Tecnai Arctica cryo-TEM that was equipped with a 200 kV Schottky field emission gun. Microscopy was carried out at −175 °C sample temperature by using the low-dose protocol of the microscope at calibrated ×23.5 k or ×39 k primary magnification. Data collection and analysis were carried out with ENAM v.2 image processing software.

Mechanical tests. For mechanical tests, samples were prepared according to the ASTM D3822 standard by using acrylic tensile test frames with 25 mm gauge length and by attaching single fibres or fibre bundles with epoxy resin. Sample were tested with an Instron 5566 tensile tester that was equipped with a 2525 Series Drop-through 10 N load cell and pneumatic grips. Data collection and analysis were carried out with Bluehill v.3 software.

Small-angle X-ray scattering. SAXS experiments were performed in the 4C SAXS beamline of the Pohang Accelerator Laboratory in Korea. Keratin SAXS samples were transferred to quartz capillaries (with 1.5 mm outside diameter and 0.01 mm wall thickness) (Charles Supper Company) and centrifuged for 4 h at 2,500 r.p.m. The scattering data were acquired with X-ray beam illumination at a sample-to-detector distance of 5 m. The samples were measured for only 60 s to prevent radiation damage of the samples. 2D SAXS data were averaged into 1D curves of scattering intensity versus q. The backgrounds were set as a polynomial function that passed through the scattering minima of each SAXS curve.

Wide-angle X-ray scattering. WAXS data were acquired with a SAXSLab instrument (CMSE X-ray facility at the Massachusetts Institute of Technology) that was equipped with a Rigaku MicroMax-002 X-ray source and Osmic staggered parabolic multilayer optics. A wavelength of 45 keV (0.66 mA, 0.0275 nm) was chosen. A DECTRIS PILATUS3 R 300K detector was positioned 109.1 mm from the sample. The beam size at the sample was approximately 900 µm × 900 µm. Samples were prepared by gluing a bundle of (approximately 40) parallel fibres on an acrylic frame, and the frame was positioned perpendicular to the beam and with the longitudinal fibre axis parallel to the meridian axis of the detector. Data collection and analysis were carried out with SAXSGUI v.2.23.09 and RAW v.1.5.1 software.

Statistics and reproducibility. Experimental errors are calculated as the standard error of the mean, with n referring to the number of analysed samples and reported in the figure legends.

Reporting Summary. Further information on research design is available in the Nature Research Reporting Summary linked to this article.

Data availability

All produced data that support this study are included in this published article and its supplementary information files. Data points for the mechanical tests are provided as source data files. Additional data are available from the corresponding author upon request. Source data are provided with this paper.

Acknowledgements

We thank the Wyss Institute for Biologically Inspired Engineering at Harvard University for ongoing support throughout this project. We also thank the Center for Nanoscale Systems at Harvard University, in particular S. Stoilova-McPhie and A. McClelland for their assistance in the use of the cryo-TEM and Raman spectrometer, respectively. The Center for Nanoscale Systems is a member of the National Nanotechnology Infrastructure Network, which is supported by the National Science Foundation under award no. 1541959. This work was partially funded by the Materials Research Science and Engineering Center of Harvard University under National Science Foundation award no. DMR-1420570. We thank the X-ray Diffraction Shared Experimental Facility at the Massachusetts Institute of Technology, and in particular C. Settens for his assistance during the WAXS experiments. We thank M. Rosnach for his graphic design support. SAXS experiments were supported by the Korean Atomic Energy Research Institute through National Research Foundation grant nos. 2017M2A2A6A01071190 and 2018R1A2B3001690. Finally, we acknowledge the financial support from the Basic Science Research Program of the National Research Foundation (grant nos. 2018R1A6A1A03024940 and 2019R1A2C2084638), which is funded by the Ministry of Science and ICT (Information and Communication Technology) of Korea.

Author contributions

L.C. and K.K.P. conceived and designed the work. L.C. implemented the keratin extraction, fibre spinning and 3D printing protocols. J.L., M.C.C. and K.S. conducted the SAXS experiments and related data analysis and interpretation. G.M.G. and Q.L. carried out the rheological measurements and related data analysis. C.O.C., G.M.G. and L.C. carried out the tensile tests. L.C. conducted the Raman spectroscopy, polarized light microscopy, SDS–PAGE, WAXS, circular dichroism spectrometry, SEM, cryo-TEM and related data analysis and interpretation. S.C. and R.G. designed the 3D-printed structures. L.C. wrote the manuscript. Q.L., G.M.G., C.O.C., K.S. and K.K.P. edited the manuscript. All authors discussed the results.

Competing interests

The authors declare no competing interests.

Additional information

Supplementary information is available for this paper at https://doi.org/10.1038/s41563-020-0789-2.

Correspondence and requests for materials should be addressed to K.K.P.

Reprints and permissions information is available at www.nature.com/reprints.

nature research

Corresponding author(s): Kevin Kit Parker

Last updated by author(s): Jun 23, 2020

Reporting Summary

Nature Research wishes to improve the reproducibility of the work that we publish. This form provides structure for consistency and transparency in reporting. For further information on Nature Research policies, see our Editorial Policies and the Editorial Policy Checklist.

Statistics

For all statistical analyses, confirm that the following items are present in the figure legend, table legend, main text, or Methods section.

n/a	Confirmed	
☐	☒	The exact sample size (*n*) for each experimental group/condition, given as a discrete number and unit of measurement
☐	☒	A statement on whether measurements were taken from distinct samples or whether the same sample was measured repeatedly
☒	☐	The statistical test(s) used AND whether they are one- or two-sided *Only common tests should be described solely by name; describe more complex techniques in the Methods section.*
☒	☐	A description of all covariates tested
☒	☐	A description of any assumptions or corrections, such as tests of normality and adjustment for multiple comparisons
☐	☒	A full description of the statistical parameters including central tendency (e.g. means) or other basic estimates (e.g. regression coefficient) AND variation (e.g. standard deviation) or associated estimates of uncertainty (e.g. confidence intervals)
☒	☐	For null hypothesis testing, the test statistic (e.g. *F*, *t*, *r*) with confidence intervals, effect sizes, degrees of freedom and *P* value noted *Give P values as exact values whenever suitable.*
☒	☐	For Bayesian analysis, information on the choice of priors and Markov chain Monte Carlo settings
☒	☐	For hierarchical and complex designs, identification of the appropriate level for tests and full reporting of outcomes
☒	☐	Estimates of effect sizes (e.g. Cohen's *d*, Pearson's *r*), indicating how they were calculated

Our web collection on statistics for biologists contains articles on many of the points above.

Software and code

Policy information about availability of computer code

Data collection	Cryo-TEM image processing software: EMAN2 Scanning electron microscopy: SmartSEM Wide Angle X-ray Scattering: SAXSGUI v2.23.09 Circular dichroism: SpectraManager 2 UV spectrometry: Cary WinUV Rheology: Trios v4.4.1 (TA instruments) Raman spectroscopy: LabSpec v6.4.4 Tensile tests: Instron Bluehill v3
Data analysis	Cryo-TEM image processing software: EMAN2 Scanning electron microscopy: SmartSEM Wide Angle X-ray Scattering: SAXSGUI v2.23.09 and RAW v1.5.1 Small Angle X-ray Scattering: MATLAB Rheology: Trios v4.4.1 (TA instruments) Tensile tests: Instron Bell v3 Raman spectroscopy: LabSpec v6.4.4 UV spectrometry: Cary WinUV

For manuscripts utilizing custom algorithms or software that are central to the research but not yet described in published literature, software must be made available to editors and reviewers. We strongly encourage code deposition in a community repository (e.g. GitHub). See the Nature Research guidelines for submitting code & software for further information.

Data

Policy information about availability of data

All manuscripts must include a data availability statement. This statement should provide the following information, where applicable:

- Accession codes, unique identifiers, or web links for publicly available datasets
- A list of figures that have associated raw data
- A description of any restrictions on data availability

All produced data that support this study are included in this published article and its supplementary information files. Data points for the mechanical tests are provided as source data files. Additional data are available from the corresponding authors upon request.

Field-specific reporting

Please select the one below that is the best fit for your research. If you are not sure, read the appropriate sections before making your selection.

☒ Life sciences ☐ Behavioural & social sciences ☐ Ecological, evolutionary & environmental sciences

For a reference copy of the document with all sections, see nature.com/documents/nr-reporting-summary-flat.pdf

Life sciences study design

All studies must disclose on these points even when the disclosure is negative.

Sample size	No sample size calculation was performed. Sample size (n) for statistical analysis was determined to reflect the standards in published literature. Mechanical tests: n = 3 independent measured fibers, as reported in Misarez et al. Nat. Mater. 8, 910-916 (2009). (Ref. 13 main manuscript). UV analysis (The Bradford assay for extracted keratin concentration): n = 3 independent measured aliquots as reported in the Bradford assay kit protocol and in Palanza et al. JIEMS 4, 1-8, (2016) (DOI: 10.1177/2326409816649600). Rheology measurements: n = 3 independent measurements of batches, as reported in Nicole M. James et al. Nat. Mater. 17, 965-970 (2018) (https://doi.org/10.1038/s41563-018-0175-5).
Data exclusions	No samples were excluded from analysis.
Replication	All experiments were replicated successfully at least three times. The number of replicates for each experiment is noted in the respective figure caption.
Randomization	No specific random sample allocation method was used in this study, as randomization is not relevant for the material characterization carried out in this study. No participants groups were involved in the study.
Blinding	Blinding was not applied to any of the performed studies, as no participants groups were involved in the study.

Reporting for specific materials, systems and methods

We require information from authors about some types of materials, experimental systems and methods used in many studies. Here, indicate whether each material, system or method listed is relevant to your study. If you are not sure if a list item applies to your research, read the appropriate section before selecting a response.

Materials & experimental systems

n/a	Involved in the study
☒	☐ Antibodies
☒	☐ Eukaryotic cell lines
☒	☐ Palaeontology and archaeology
☒	☐ Animals and other organisms
☒	☐ Human research participants
☒	☐ Clinical data
☒	☐ Dual use research of concern

Methods

n/a	Involved in the study
☒	☐ ChIP-seq
☒	☐ Flow cytometry
☒	☐ MRI-based neuroimaging